Lithium Batteries

International Edition: DOI: 10.1002/anie.201814324
German Edition: DOI: 10.1002/ange.201814324

Stabilizing Lithium into Cross-Stacked Nanotube Sheets with an Ultra-High Specific Capacity for Lithium Oxygen Batteries

Lei Ye[+]*, Meng Liao*[+]*, Hao Sun, Yifan Yang, Chengqiang Tang, Yang Zhao, Lie Wang, Yifan Xu, Lijian Zhang, Bingjie Wang, Fan Xu, Xuemei Sun, Ye Zhang,* Hongjie Dai, Peter G. Bruce, and Huisheng Peng**

Abstract: *Although lithium–oxygen batteries possess a high theoretical energy density and are considered as promising candidates for next-generation power systems, the enhancement of safety and cycling efficiency of the lithium anodes while maintaining the high energy storage capability remains difficult. Here, we overcome this challenge by cross-stacking aligned carbon nanotubes into porous networks for ultrahigh-capacity lithium anodes to achieve high-performance lithium–oxygen batteries. The novel anode shows a reversible specific capacity of 3656 mAh g*$^{-1}$*, approaching the theoretical capacity of 3861 mAh g*$^{-1}$ *of pure lithium. When this anode is employed in lithium–oxygen full batteries, the cycling stability is significantly enhanced, owing to the dendrite-free morphology and stabilized solid–electrolyte interface. This work presents a new pathway to high performance lithium–oxygen batteries towards practical applications by designing cross-stacked and aligned structures for one-dimensional conducting nanomaterials.*

With the rapid advance of modern electronics, grid storage, and electric vehicles, the need for high-energy-density batteries becomes more urgent and important than at any time in the past.[1] Lithium–oxygen (Li–O_2) batteries, having a high theoretical energy density of 3505 Wh kg^{-1}, are widely recognized as promising candidates.[2,3] A Li–O_2 battery usually consists of a lithium metal anode, an electrolyte and a porous air electrode. Thus far, much attention has been paid to electrolyte and air electrodes to enhance the electrochemical properties of Li–O_2 batteries to the expected level.[4–6] However, the problematic lithium metal anode holds back the pace of realization of practical Li–O_2 batteries (Figure 1 a). The formation of Li dendrites during discharge/charge processes leads to serious safety problems.[7–13] The instability of the recurring Li accommodation and Li/electrolyte interface also results in side reactions and loss of Li during cycling, which degrades the cycling efficiency of Li–O_2 batteries with poor performances.[14,15]

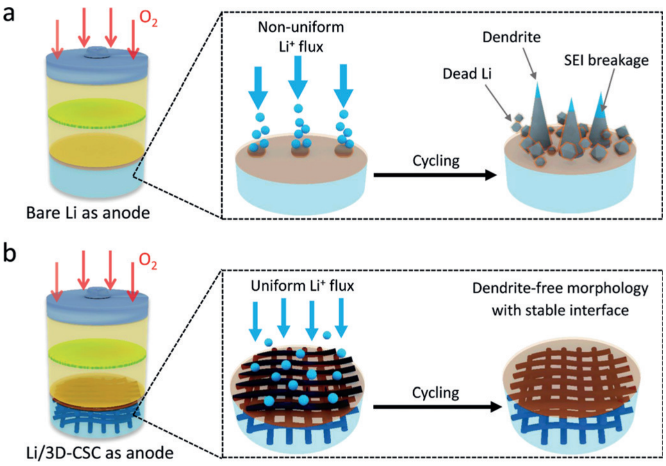

Figure 1. Depiction of the structure change for different Li metal anodes in Li–O_2 batteries: a) In a conventional Li metal anode (blue cylinder), Li$^+$ (blue particles) aggregates at the tips of Li protuberances, which leads to the formation of Li dendrites, "dead Li", SEI breakage (orange), and an O_2 crossover effect after cycling. b) In a Li/3D-CSC anode (black), Li is likely to deposit homogenously and grow on the 3D-CSC scaffold, forming a smooth interface with high stability.

To solve these problems, some attempts have been made to develop protective films on the surface of the Li metal to enhance the stability of Li/electrolyte interfaces[16,17] and alloyed Li anodes such as lithiated silicon and Li/graphene composites are explored to replace the Li metal.[18–22] However, the necessity to introduce a second component in both methods largely decreases the loading capacity and utilization ratio of reactive Li with low specific capacities, which deviates from the goal of high energy densities in Li–O_2 batteries. Therefore, it remains a challenge to improve the safety and cycling efficiency while maintaining the high specific capacity.

We have developed a three-dimensional cross-stacked carbon nanotube network (3D-CSC) with deposited Li as an

---

[*] L. Ye,[+] M. Liao,[+] C. Tang, Y. Zhao, L. Wang, Y. Xu, L. Zhang,
Dr. B. Wang, Dr. X. Sun, Dr. Y. Zhang, Prof. H. Peng
State Key Laboratory of Molecular Engineering of Polymers
Department of Macromolecular Science, and Laboratory of Advanced Materials, Fudan University
Shanghai 200438 (China)
E-mail: zhangye13@fudan.edu.cn
penghs@fudan.edu.cn

Dr. H. Sun, Prof. H. Dai
Department of Chemistry, Stanford University
Stanford, CA 94305 (USA)

Y. Yang, Dr. F. Xu
Institute of Mechanics and Computational Engineering
Department of Aeronautics and Astronautics, Fudan University
Shanghai 200433 (China)

Prof. P. G. Bruce
Department of Materials, University of Oxford
Parks Rd, Oxford OX1 3PH (UK)

[+] These authors contributed equally to this work.

Supporting information and the ORCID identification number(s) for the author(s) of this article can be found under: https://doi.org/10.1002/anie.201814324.

effective anode (Li/3D-CSC) for high-performance Li–O_2 batteries (Figure 1b). The 3D-CSC scaffold has several notable advantages: 1) The aligned carbon nanotube (CNT) network connected by an end-to-end joining mechanism[23] is extremely lightweight (ca. 0.07 mg cm^{-2}) with low sheet resistance, affording accessibility to fabricate high-performance Li anodes with a minimized effect on capacity. 2) The expandable, porous scaffold with a large surface area facilitates uniform, dendrite-free Li deposition and mitigates the volume change for a stable cycling performance. 3) The electrochemical and mechanical stability makes it a compatible host for Li deposition, thus it is favored in a wide variety of applications such as Li–O_2 batteries. Owing to these merits, the Li/3D-CSC anode delivers a reversible specific capacity up to 3656 mAh g^{-1}, approaching the theoretical specific capacity of pure Li metal (3861 mAh g^{-1}). Based on the Li/3D-CSC anode, the obtained Li–O_2 battery shows a five-fold enhanced cycling performance of that based on commonly used bare Li foil anodes.

The 3D-CSC was comprised of aligned CNT sheets that were drawn from a spinnable CNT and then cross-stacked layer by layer orthogonally.[23] The scaffold exhibited a high specific surface area of 424.4 m^2 g^{-1} (Supporting Information, Figure S1) and an interconnected architecture with micrometer-sized voids of periodic interval (Figure S2). These voids enabled Li ions to access the inner space of the 3D-CSC and benefit from the full utilization of its large electroactive surface (Figure S3).[9] Furthermore, the 3D-CSC showed both high flexibility and mechanical strength (Figure S4), keeping its promise for the continuous production of Li–O_2 batteries, which require the capability to withstand folding, rolling, and the other deformations.[24] The 3D-CSC can be used in a large size or cut into small electrodes without additional current collectors. In this study, for example, a diameter of about 10 mm and a thickness of about 1 μm was used.

Li/3D-CSC anodes were prepared by electrodeposition of metallic Li into the 3D-CSC (Figure 2a and Supporting Information, Figure S5). With the deposition of Li, a characteristic peak corresponding to the (110) plane of the Li metal appeared at 36.4° in the X-ray diffraction (XRD) pattern.[16] Lithium can be stripped reversibly from the 3D-CSC and the characteristic Li peak vanished after 100 Li-plating/stripping cycles (Figure 2b). The morphology evolution of the Li/3D-CSC anode was also traced by scanning electron microscopy (SEM). The pristine 3D-CSCs demonstrated a porous structure with micrometer-sized voids and a thicknesses of approximately 1.1 μm (Figure 2c,d). The transmission electron micrograph (TEM) images of the initially Li-plated 3D-CSCs showed deposition in the form of Li nanoparticles on the CNT surface (Supporting Information, Figure S6). After electroplating Li for 1 h (areal load of 1 mAh cm^{-2}), Li particles with diameters of tens of nanometers emerged on the cross-stacked CNT bundles in a uniform manner (Figure 2e,f and Supporting Information, Figure S7). After electroplating Li for 2 h (2 mAh cm^{-2}), the cross-stacked structure was almost invisible at the top surface of the Li/3D-CSC, and larger Li aggregates gradually emerged (Figure 2g). Li was not only deposited on the CNT bundle, but also evenly plated

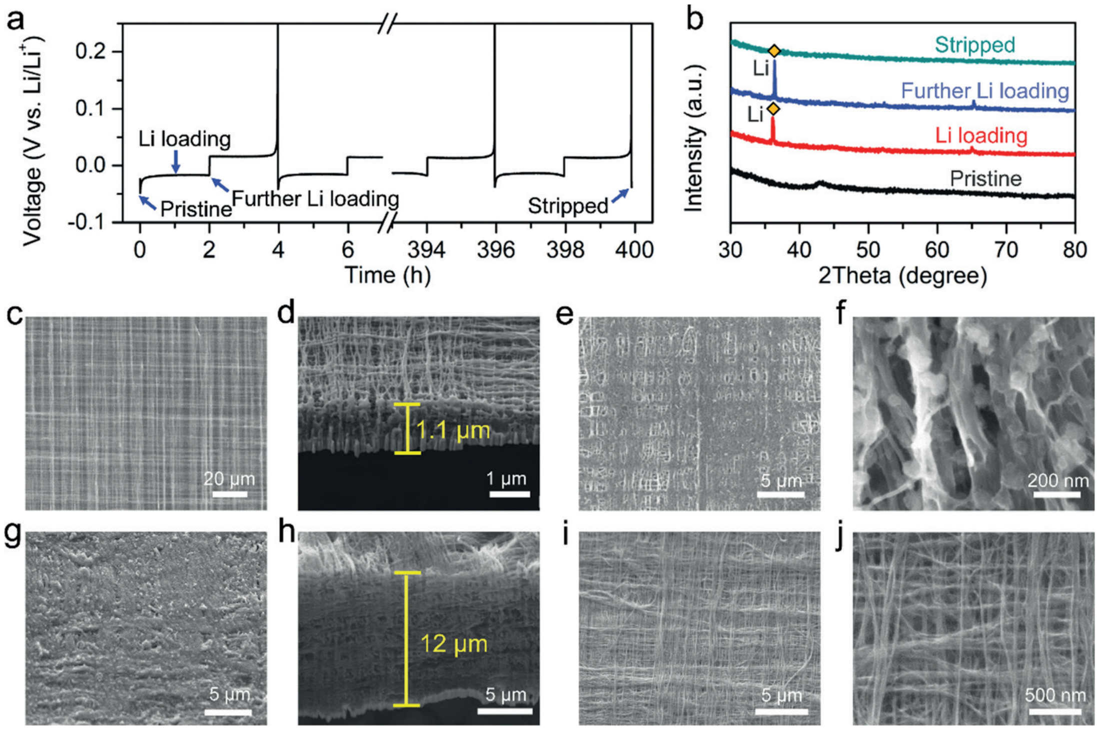

Figure 2. Characterization of the Li/3D-CSC anode: a) Voltage profiles of the Li/3D-CSC anode during depositing and stripping with four representative states labeled. b) XRD patterns for the Li/3D-CSC anode at the four states shown in (a). c),d) Top and cross-sectional SEM images of the pristine 3D-CSC. e),f) Top morphology of the Li/3D-CSC in the "Li loading" state in two degrees of magnification. g),h) Top and cross-sectional SEM images of the Li/3D-CSC in the "further Li loading" state. i),j) Top morphology of the stripped 3D-CSC in the "stripped" state in two degrees of magnification.

in the voids among the CNT bundles. The robust CNT scaffold was capable to withstand the volume change induced by Li deposition and the thickness of the Li/3D-CSC was increased to about 12 μm (Figure 2h). Note that after 100 cycles of Li plating/stripping, the originally cross-stacked structure of the 3D-CSC was restored at the end of Li-stripping (Figure 2i,j and Supporting Information, Figure S8), indicating a high mechanical durability against volume changes of the scaffold. On the contrary, dendritic Li shot out on the conventional planar Cu foil current collector after 10 cycles of Li plating/stripping (Supporting Information, Figure S9).

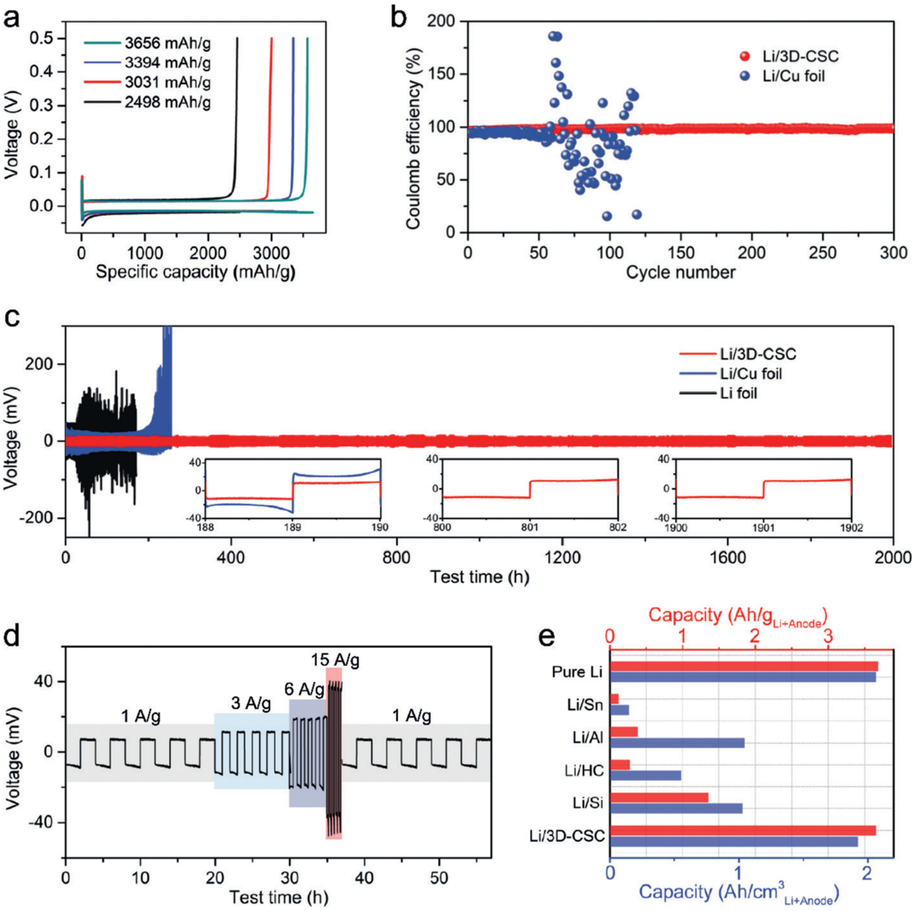

Figure 3. Electrochemical characterization of the Li/3D-CSC anode: a) Li storage capacities of the 3D-CSC at 2498 $\mathrm{mAh\,g^{-1}}$ (0.5 $\mathrm{mAh\,cm^{-2}}$) to 3656 $\mathrm{mAh\,g^{-1}}$ (5 $\mathrm{mAh\,cm^{-2}}$). b) Comparison of the Coulomb efficiency of the Li/3D-CSC and Li/Cu foil (areal capacity: 1 $\mathrm{mAh\,cm^{-2}}$, current density: 1 $\mathrm{mA\,cm^{-2}}$). c) Voltage profiles of Li plating/stripping in three symmetric cells (Li/3D-CSC, Li/Cu foil and Li foil) at 1 $\mathrm{mA\,cm^{-2}}$ for 1 $\mathrm{mAh\,cm^{-2}}$. d) Rate performance of the Li/3D-CSC anode during continuous cycling at current densities increasing from 1 to 15 $\mathrm{A\,g^{-1}}$. e) Comparison of the gravimetric and volumetric capacity of the Li/3D-CSC anode with other anodes in Li–O_2 batteries.

To evaluate the electrochemical performance of the Li/3D-CSC anode, symmetrical coin cells based on 3D-CSC electrodes were assembled. Before the electroplating process, the 3D-CSC was first treated by an activation method (for details, see Experimental Section and Supporting Information, Figure S10) to remove surface impurities and form the initial solid–electrolyte interface (SEI; Figure S11 and Table S1), which is important for a high initial cycle Coulomb efficiency (CE).[25] Then, by increasing the electroplating time of Li, the Li/3D-CSC could enable gravimetric capacities between 2498 and 3656 $\mathrm{mAh\,g^{-1}}$ (or between 0.5 and 5 $\mathrm{mAh\,cm^{-2}}$, see Figure 3a). A small voltage gap of 32 mV between the Li plating and stripping curves was observed for 2498 $\mathrm{mAh\,g^{-1}}$, which rose to 38 mV at a ceiling specific capacity of 3656 $\mathrm{mAh\,g^{-1}}$ (Figure 3a), very close to the theoretical capacity of pure lithium (3861 $\mathrm{mAh\,g^{-1}}$). The specific capacity could be well maintained at 3 $\mathrm{A\,g^{-1}}$ (or 1 $\mathrm{mA\,cm^{-2}}$) for at least 100 cycles with a CE of over 95% (Supporting Information, Figure S12). Please note here that the thickness of the Li/3D-CSC increased with the increasing Li capacity (Figure S13). For a typical 3D-CSC (initial thickness of 1.1 μm), the maximum Li capacity is 3656 $\mathrm{mAh\,g^{-1}}$ or 5 $\mathrm{mAh\,cm^{-2}}$ (thickness of about 27 μm, Figures S14 and S15). By fabricating a 3D-CSC substrate with increased initial thickness, a higher Li deposition capacity could be furthermore achieved (Figure S16).

To systematically evaluate the role of the 3D-CSC during cycling, a conventional Cu foil was introduced as a control sample. At a current density of 3 $\mathrm{A\,g^{-1}}$ with a capacity of 3031 $\mathrm{mAh\,g^{-1}}$, the plating/stripping profiles of the Li/3D-CSC kept their flatness and showed high overlap for at least 300 cycles (Supporting Information, Figure S17) with a CE around 99% (Figure 3b and Supporting Information, Figure S18). In a stark contrast to this, the CE of the planar Cu foil rapidly decayed to < 90% and then intensively oscillated, probably due to the recurring corrosion by Li dendrites (Figure S19). Next, to probe the galvanostatic cycling performance of the Li/3D-CSC, a long-time cycling test was conducted at a current density of 3 $\mathrm{A\,g^{-1}}$ and a Li stripping/plating of 1 h in each cycle (Figure 3c). Noticeably, the Li/3D-CSC showed a low overpotential of about 12 mV without fluctuation for at least 2000 h. On the contrary, the voltage profiles of the symmetrical cells from Li/Cu and Li/Li foils exhibited intensive overpotential bumps within 200 h, indicative of the spatial variation in localized reaction kinetics on the electrode surface due to the dynamic dendritic propagation (Figure 3c and Supporting Information, Figure S20). Compared with the electrochemical impedance spectroscopy curves for Li/Cu and Li/Li foils, the considerably lower interfacial impedance charge transfer resistance from the Li/3D-CSC suggested more favorable Li plating/stripping kinetics and better reversibility (Figures S21–S23) as well. The rate performance of the Li/3D-CSC was then tested by cycling at a spectrum of current densities (Figures 3 d and S24). The voltage hysteresis increased with increasing current densities from 1 to 15 $A\,g^{-1}$ and kept steady at a high rate of 15 $A\,g^{-1}$ (Figure 3 d), as aligned CNT bundles favor Li-ion diffusion during cycling.[25,26]

The results presented above indicate that the recurring Li accommodation has been significantly improved for the 3D-CSC scaffold: The conducting scaffold with high specific surface area facilitates not only homogeneous Li nucleation but also a dendrite-free deposition behavior during the later Li growth. At the beginning of Li plating, Li ions in the electrolyte migrate towards the surface of the 3D-CSC, driven by the electric field and the concentration gradient.[27] When the Li^+ flux reaches the 3D-CSC, it would be homogenously decentralized by the conductive scaffold with a high surface area, acquiring electrons and forming nucleation sites. The 3D-CSC electrode exhibited much lower nucleation overpotentials at increasing current densities (that is, between 26 and 79 mV at current densities between 0.01 and 2.0 $mA\,cm^{-2}$) compared to conventional current collectors (55 to 139 mV, Supporting Information, Figure S25), verifying a lowered resistance for Li deposition.[27] Simulation of the electric field in scale models, performed by Ansoft Maxwell, confirmed the improved Li^+ flux uniformity in the 3D-CSC scaffold during the Li deposition after the initial nucleation (Figure 4 a–d). The uniform deposition of Li onto the 3D-CSC was further confirmed by atomic force microscopy and showed both a smooth morphology and a lower surface potential (Figure S26). Furthermore, the robust cross-stacked structure is responsible for the enhanced stability of the 3D-CSC anode as well (Figure S27). One CNT bundle could be restricted by neighboring ones, avoiding the contraction of the scaffold upon electrolyte soaking, thereby enabling a higher durability to decrease the SEI breakage and Li protrusion from the recurring volume change during cycling.[28,29] The von-Mises stress distribution demonstrated a tensile tolerance in the 3D-CSC enhanced by about 60 % compared to other CNT-based scaffolds (Figure 4 e–g), indicating the necessity of the cross-stacked structure. The above combined advantages of the Li/3D-CSC contribute to the beneficial specific capacity of 3656 $mAh\,g^{-1}$ (or 1923 $mAh\,cm^{-3}$, Figure 3 e and Supporting Information, Figure S28 and Table S2).

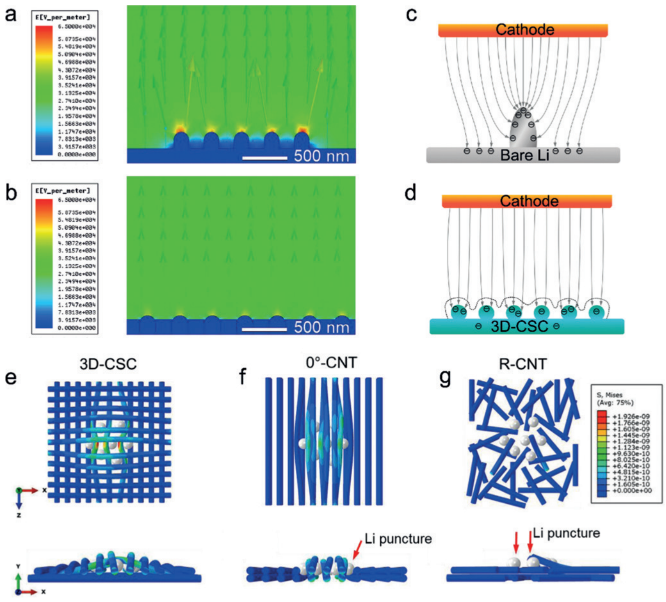

Figure 4. Simulations showing the homogenous electric field distribution and enhanced mechanical durability in the 3D-CSC: a),b) Models of the electric field of a) conventional Li foil and b) the 3D-CSC. c),d) Schematic diagrams of Li deposition behavior on the surfaces of c) Cu foil and d) the 3D-CSC. e)–g) von-Mises stress distribution of the Li protrusions (shown as silver particles) against different CNT scaffolds at a fixed Li deposition height for e) the 3D-CSC, f) a stacked CNT sheet, and g) a randomly dispersed CNT film.

Inspired by the successful construction of ultrahigh-capacity Li/3D-CSC anodes, we then examined their effectiveness in Li–O_2 full batteries with an ether-based electrolyte. Figure 5 a,b shows the discharge-charge curves of two Li–O_2 batteries in which the Li/3D-CSC and a bare Li foil with the same amount of Li served as the anode. A specific capacity cut-off of 1000 $mAh\,g^{-1}$ was set for cyclic tests at 2000 $mA\,g^{-1}$. Impressively, the Li–O_2 full batteries using the Li/3D-CSC anode exhibited high cycling performances for at least 260 cycles, with highly overlapping discharge and charge plateaus (Figure 5 a). The discharge product on the cathode turned out to be a Li_2O_2 nanosheet (Supporting Information, Figure S29). Notably, the ultimate charge voltages demonstrated negligible variations compared with the initial state, suggesting alleviated polarization and electrolyte-related side reactions. In contrast, the Li–O_2 full batteries using the bare Li foil anode were unable to continuously cyclize for even 50 cycles, showing increasing charge plateaus and ill-defined discharge plateaus (Figure 5 b). Furthermore, the cycling performance of a Li–O_2 battery using the Li/3D-CSC shows a five-fold enhancement compared to the one using a bare Li foil (Figure 5 c).

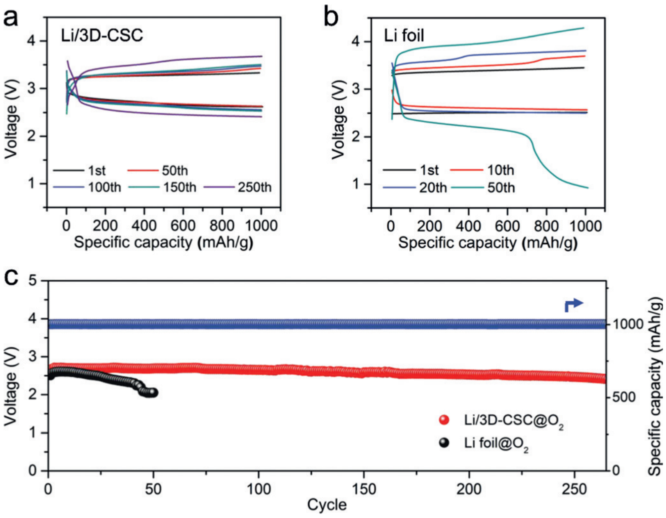

Figure 5. Electrochemical performance of Li–O_2 full batteries based on conventional Li and Li/3D-CSC anodes: a),b) Cyclic performances of Li–O_2 batteries with a) 3D-CSC and b) bare Li foil anodes at 2000 $mA\,g^{-1}$ under a capacity cut-off of 1000 $mAh\,g^{-1}$. c) Corresponding cycling performances of the Li–O_2 full batteries in (a) and (b).

To understand the high performance of the Li/3D-CSC in Li–O_2 batteries, we investigated the morphology evolution of the two anode surfaces after cycling. Prior to the first charging, both the Li/3D-CSC and the Li foil demonstrated relatively smooth surfaces. The surface of the Li/3D-CSC anode remained smooth without Li dendrite formation after cycling (Figure 6 a, right) whereas the surface of the bare Li foil anode became rougher and dendritic Li and "dead Li" piling up into a huge block could be observed after charging and discharging (Figure 6 a, left and Supporting Information, Figure S30), which leads to perpetual lithium depletion. Moreover, the formation of dendritic Li kept breaking as-formed SEI and the newly exposed Li spontaneously reacted with the electrolyte, leading to the formation of unstable and thick SEIs and depletion of the electrolyte. Fourier transform infrared (FTIR) spectroscopy and X-ray photoelectron spectroscopy further verified this. Two kinds of anodes were extracted from the full batteries and washed after cycling for a comparative study. In comparison to the bare Li anode, the characteristic peaks of surface groups like carbonyl (C═O) (ca. 1720 cm^{-1}), C–O (ca. 1480 cm^{-1}) and C–F (1210 cm^{-1}) were very small in FTIR spectra of the Li/3D-CSC anode,[15] indicating few byproducts stemming from electrolyte corrosion in Li–O_2 batteries (Figure 6 b). The general elemental compositionof the SEIs was investigated by X-ray photoelectron spectroscopy of the C 1s, O 1s, F 1s, and S 2p states (Figure 6 c,d; Supporting Information, Figure S31). For the bare Li anode, larger proportions of Li_2CO_3 and LiOH were evident from peaks at 289.5 eV (C 1s, Li_2CO_3) and 532.0 eV (O 1s, LiOH).[17,19] In contrast, smaller proportions of Li_2CO_3 and LiOH were observed for the Li/3D-CSC anode, along with an intensified C–C peak originating from the CNT scaffold.

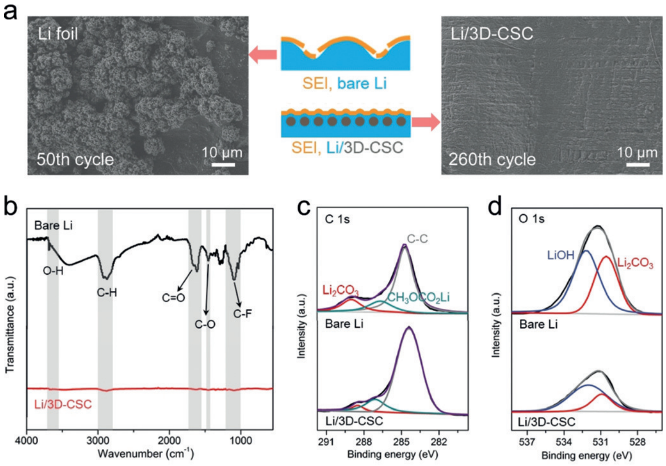

Figure 6. Characterization of conventional Li and Li/3D-CSC anodes disassembled from Li–O_2 full batteries after cycling: a) SEM images and schematic illustrations showing the morphologies of bare Li foil and Li/3D-CSC anodes after cycling. b) FTIR absorption spectrum of the bare Li foil and Li/3D-CSC anodes after cycling. The Li/3D-CSC anode is less contaminated than bare Li. c),d) XPS analysis (C 1s and O 1s) of the SEI on conventional Li and Li/3D-CSC anodes after cycling in Li–O_2 batteries.

Based on the results presented above, we propose that the dendrite-free morphology along with the stable SEI induced by the 3D-CSC can account for the enhanced cycling performance of the Li–O_2 batteries. In the bare Li foil anode, the newly exposed Li, induced by dendrite growth, tended to reduce the electrolyte to byproducts (that is, precipitates containing O, C, and F). Here, the introduced 3D-CSC effectively suppresses dendrite formation and mitigates the volume change during cycling, resulting in a decrease of side reactions and byproducts on the anode surface. Moreover, it was reported that expandable layered scaffolds are capable of maintaining as-formed SEI.[8,10] With the stabilized SEI of the Li/3D-CSC, SEI cracking and further contamination during cycling can be highly suppressed, leading to much less polarization and low internal resistance (Figure 5 a,b and Supporting Information, Figures S32 and S33). This feature is beneficial to both battery life and rate performance (Figure S34) of resulting Li–O_2 batteries.

In conclusion, we demonstrated a general and promising strategy by designing a cross-stacked and porous structure for ultrahigh-capacity Li anodes that can be applied to a variety of one-dimensional conducting nanomaterials with the combined advantages of a high specific surface area, periodic porosity, a low mass density and high mechanical durability. The presented Li/3D-CSC anode showed an unexpected specific capacity near to the theoretical value of pure Li with a high stability. When used in Li–O_2 batteries, the cycling stability of this anode was significantly enhanced thanks to the dendrite-free morphology and stabilized SEI. This work may have opened up a new avenue to fully implement the advantages of Li–O_2 batteries into future applications.

Acknowledgements

This work was supported by MOST (2016YFA0203302), NSFC (21634003, 51573027, 51673043, 21604012, 21805044, 21875042, 11602058, 11872150), STCSM (16JC1400702, 17QA1400400, 18QA1400700, 18QA1400800), SHMEC (2017-01-07-00-07-E00062), SEDF (16CG01) and Yanchang Petroleum Group. Part of the sample fabrication was performed at Fudan Nano-fabrication Laboratory.

Conflict of interest

The authors declare no conflict of interest.

Keywords: carbon nanotubes · lithium dendrites · lithium metal anodes · lithium oxygen batteries

How to cite: *Angew. Chem. Int. Ed.* **2019**, *58*, 2437–2442
Angew. Chem. **2019**, *131*, 2459–2464

---

[1] P. G. Bruce, S. A. Freunberger, L. J. Hardwick, J. M. Tarascon, *Nat. Mater.* **2011**, *11*, 19–29.
[2] C. Xia, C. Y. Kwok, L. F. Nazar, *Science* **2018**, *361*, 777–781.
[3] T. Liu, M. Leskes, W. Yu, A. J. Moore, L. Zhou, P. M. Bayley, G. Kim, C. P. Grey, *Science* **2015**, *350*, 530–533.

[4] P. Tan, Z. Wei, S. Wei, T. S. Zhao, X. Zhu, *Energy Environ. Sci.* **2016**, *9*, 1783 – 1793.

[5] J. Wang, Y. Yin, T. Liu, X. Yang, Z. Chang, X. Zhang, *Nano Res.* **2018**, *11*, 3434 – 3441.

[6] Y. Chen, X. Gao, L. Johnson, P. Bruce, *Nat. Commun.* **2018**, *9*, 767 – 772.

[7] D. Lin, Y. Liu, Y. Cui, *Nat. Nanotechnol.* **2017**, *12*, 194 – 206.

[8] D. Lin, Y. Liu, Z. Liang, H. W. Lee, J. Sun, H. Wang, K. Yan, J. Xie, Y. Cui, *Nat. Nanotechnol.* **2016**, *11*, 626 – 632.

[9] C. P. Yang, Y. X. Yin, S. F. Zhang, N. W. Li, Y. G. Guo, *Nat. Commun.* **2015**, *6*, 8058 – 8066.

[10] Z. Sun, S. Jin, H. Jin, Z. Du, Y. Zhu, A. Cao, H. Ji, L. Wan, *Adv. Mater.* **2018**, *30*, 1800884.

[11] S. Jiao, J. Zheng, Q. Li, X. Li, M. H. Engelhard, R. Cao, J. G. Zhang, W. Xu, *Joule* **2018**, *2*, 110 – 124.

[12] P. Zou, Y. Wang, S. W. Chiang, X. Wang, F. Kang, C. Yang, *Nat. Commun.* **2018**, *9*, 464 – 472.

[13] C. Yang, L. Zhang, B. Liu, S. Xu, T. Hamann, D. Mcowen, J. Dai, W. Luo, Y. Gong, E. D. Wachsman, *Proc. Natl. Acad. Sci. USA* **2018**, *115*, 201719758 – 201719763.

[14] H. Song, H. Deng, C. Li, N. Feng, P. He, H. Zhou, *Small Methods* **2017**, *1*, 1700135 – 1700149.

[15] J. Xu, Q. Liu, Y. Yu, J. Wang, J. Yan, X. Zhang, *Adv. Mater.* **2017**, *29*, 1606552 – 1606557.

[16] M. Asadi, B. Sayahpour, P. Abbasi, A. T. Ngo, K. Karis, J. R. Jokisaari, C. Liu, B. Narayanan, M. Gerard, P. Yasaei, *Nature* **2018**, *555*, 502 – 506.

[17] Q. Liu, J. Xu, S. Yuan, Z. Chang, D. Xu, Y. Yin, L. Li, H. Zhong, Y. Jiang, J. Yan, *Adv. Mater.* **2015**, *27*, 5241 – 5247.

[18] Y. Zhang, Y. Jiao, L. Lu, L. Wang, T. Chen, H. Peng, *Angew. Chem. Int. Ed.* **2017**, *56*, 13741 – 13746; *Angew. Chem.* **2017**, *129*, 13929 – 13934.

[19] S. Wu, K. Zhu, J. Tang, K. Liao, S. Bai, J. Yi, Y. Yamauchi, M. Ishida, H. Zhou, *Energy Environ. Sci.* **2016**, *9*, 4352 – 4361.

[20] D. Hirshberg, D. Sharon, L. L. E. De, M. Afri, A. A. Frimer, W. J. Kwak, Y. K. Sun, D. Aurbach, *ACS Appl. Mater. Interfaces* **2017**, *9*, 4352 – 4361.

[21] Z. Guo, X. Dong, Y. Wang, Y. Xia, *Chem. Commun.* **2015**, *51*, 676 – 678.

[22] G. A. Elia, D. Bresser, J. Reiter, P. Oberhumer, Y. K. Sun, B. Scrosati, S. Passerini, J. Hassoun, *ACS Appl. Mater. Interfaces* **2017**, *7*, 22638 – 22643.

[23] K. Jiang, Q. Li, S. Fan, *Nature* **2002**, *419*, 801.

[24] L. Liu, Y. Yin, J. Li, N. Li, X. Zeng, H. Ye, Y. Guo, L. Wan, *Joule* **2017**, *1*, 563 – 575.

[25] A. O. Raji, S. R. Villegas, N. D. Kim, X. Fan, Y. Li, S. Gal, J. Sha, J. M. Tour, *ACS Nano* **2017**, *11*, 6362 – 6369.

[26] P. Chen, Y. Xu, S. He, X. Sun, S. Pan, J. Deng, D. Chen, H. Peng, *Nat. Nanotechnol.* **2015**, *10*, 1077 – 1082.

[27] R. Zhang, X. Chen, X. Chen, X. Cheng, X. Zhang, C. Yan, Q. Zhang, *Angew. Chem. Int. Ed.* **2017**, *56*, 7764 – 7768; *Angew. Chem.* **2017**, *129*, 7872 – 7876.

[28] Y. Xu, Y. Zhang, Z. Guo, J. Ren, Y. Wang, H. Peng, *Angew. Chem. Int. Ed.* **2015**, *54*, 15390 – 15394; *Angew. Chem.* **2015**, *127*, 15610 – 15614.

[29] Y. Xu, Y. Zhao, J. Ren, Y. Zhang, H. Peng, *Angew. Chem. Int. Ed.* **2016**, *55*, 7979 – 7982; *Angew. Chem.* **2016**, *128*, 8111 – 8114.

Manuscript received: December 17, 2018
Accepted manuscript online: December 21, 2018
Version of record online: January 21, 2019